Multiplexing Strategies for Monolithic Crystal PET Detector Modules

L A Pierce[1], **W C J Hunter**[1], **D R Haynor**[1], **L R MacDonald**[1], **P E Kinahan**[1], and **R S Miyaoka**[1]

L A Pierce: lapierce@uw.edu

[1]Department of Radiology, University of Washington, Seattle, WA USA

Abstract

To reduce the number of output channels and associated cost in PET detectors, strategies to multiplex the signal channels have been investigated by several researchers. This work aims to find an optimal multiplexing strategy for detector modules consisting of a monolithic LYSO scintillator coupled to a 64-channel PMT.

Methods—We apply simulated multiplexing strategies to measured data from two continuous miniature crystal element (cMiCE) detector modules. The strategies tested include standard methods such as row-column summation and its variants, as well as new data-driven methods involving the principal components of measured data and variants of those components. The detector positioning resolution and bias is measured for each multiplexing strategy and the results are compared.

Results—The mean FWHM over the entire detector was 1.23 mm for no multiplexing (64 channels). Using 16 principal component channels yielded a mean FWHM resolution of 1.21 mm, while traditional row/column summation (16 channels) yielded 1.28 mm. Using 8 principal component output channels resulted in a resolution of 1.30 mm.

Conclusion—Using the principal components of the calibration data to guide the multiplexing scheme appears to be a viable method for reducing the number of output data channels. Further study is needed to determine if the depth-of-interaction resolution can be preserved with this multiplexing scheme.

1. Introduction

The current standard for Positron Emission Tomography (PET) detectors is a block detector design that couples a discrete array of crystal scintillators to a less dense array of photomultiplier tubes (PMTs). The individual (pixelated) crystals can be optically isolated or can share some amount of light with each other (Casey & Nutt 1986)(Picard & Thompson 1994)(Dahlbom & Hoffman 1988). The detector blocks are designed so that the individual crystal of interaction can be determined by calculating a simple ratio between the light collected at the PMTs (Casey & Nutt 1986)(Picard & Thompson 1994)(Dahlbom & Hoffman 1988). The attractive feature of this design is that a few (typically 4) PMTs can be used to decode a larger array (typically 64) of crystals. This type of multiplexing helps to reduce the cost of PET detector systems. In addition, it allows crystals to be decoded that are much smaller in cross-section than the PMTs, thus supporting good spatial resolution. The block detector design works very well for whole-body, clinical imaging systems where

crystal cross-sections are about 4×4 mm^2 and the intrinsic image resolution of the imaging system is limited by the crystal size, photon acollinearity and counting statistics of the study. A limitation design for preclinical and organ specific imaging systems (where higher spatial resolution is desired) is that smaller and smaller crystal elements are required (e.g., 2×2 mm^2 or smaller). As the crystals elements get smaller, the cost for fabrication increases significantly. This is because more cutting/processing time is required and there is more crystal material wasted by the cutting process. Further, as the crystal cross-sections get smaller, smaller photosensors must be used as the finite amount of light produced by the scintillator crystal limits the number of crystals that can be decoded.

For these reasons a number of research groups, including our own, have been investigating the use of continuous, monolithic scintillation crystal detectors for high resolution PET imaging system applications (Maas et al. 2009)(Bruyndonckx et al. 2004)(Schaart et al. 2009)(Lerche et al. 2005)(Ling et al. 2007)(Ling et al. 2006). Advantages of monolithic crystal detectors designs are that they can provide near continuous sampling of the detector element that provides benefits for image reconstruction; they also can provide some depth of interaction positioning information with proper calibration of the detector unit (Ling et al. 2007)(Bruyndonckx et al. 2004)(Schaart et al. 2009); and they have low fabrication and manufacturing costs.

The main limitation to the performance of monolithic crystal detectors is that positioning near the edges of the crystals is more challenging because the light response function is distorted by edge effects. These edge effects lead to large biases in event positioning if one uses standard Anger positioning logic (Joung et al. 2002). We have developed a statistics based positioning method (Joung et al. 2002)(Ling et al. 2007), which has been shown to have improved positioning performance and reduced bias compared to Anger positioning, especially near the edge of the crystal. Other research groups have also developed their own positioning methods for monolithic crystal detectors (Joung et al. 2002)(Ling et al. 2007). In addition to using more sophisticated positioning methods, all of these detectors also use denser photosensor arrays to provide better sampling of the light response function that is used for event positioning. All the proposed techniques work well; however, for best positioning performance the signal information from all of the photosensors coupled to the monolithic crystal have generally been acquired. To reduce the number of acquisition channels (and associated costs) various multiplexing methods and data compression schemes have been investigated (Siegel et al. 1996), (Miyaoka et al. 2007), (Li et al. 2011), (Li et al. 2008), (Downie et al. 2013). However, reducing the number of output signals from the photodetectors can reduce the amount of available information to the positioning algorithm and could have a negative impact on the resolution of the detector module (Miyaoka et al. 2007).

In this paper, we focus our attention on evaluating various multiplexing strategies for the Continuous Miniature Crystal Element (cMiCE) detector modules currently under development at the University of Washington (Joung et al. 2002), (Miyaoka et al. 2011). Sample multiplexing strategies include row-column summation (e.g. from 64 to 16 channels) (Shih et al. 2009), variations on row-column summation, (Tanaka et al. 1970), Zone Triggering (Karp et al. 1986), 2nd moment of data (Lerche et al. 2005), and

compressive sensing (Olcott et al. 2011). Without multiplexing, we have achieved ~ 1.3 mm FWHM intrinsic spatial resolution for cMiCE detector modules that are comprised of a $50 \times 50 \times 8$ mm^3 LYSO crystal coupled to a 64 channel multi-anode PMT (Ling et al. 2007). We evaluate several standard methods (and their variants) and introduce a new method using the principal components of the non-multiplexed data in an effort to empirically optimize the multiplexing scheme.

2. Methods

2.1. Overview

In (Miyaoka et al. 2010), data was collected from two cMiCE detector modules for calibration. In order to evaluate the effects of multiplexing for the cMiCE modules, we revisited these datasets and subjected them to various computer-simulated multiplexing strategies. The simulated multiplexing schemes were injected into the workflow from (Miyaoka et al. 2010) as shown in Figure 1.

We describe the relevant details of the data collection in Section 2.2 and the details of the event positioning algorithm in Section 2.4. The full details of the data generation and the event positioning algorithm can be found in (Miyaoka et al. 2010) and (Ling et al. 2006).

2.2. Collection of Measured cMiCE Data

The cMiCE detector modules utilize a monolithic, continuous LYSO scintillation crystal (Saint Gobain, Newbury, OH.) with dimensions $50 \times 50 \times 8$ mm^3. This crystal is optically coupled to a 64-channel position-sensitive photomultiplier tube (H8500, Hamamatsu Photonics K.K., Japan), configured in an 8×8 array. Data was acquired using two 32-channel analog-to-digital converter (ADC) cards (N792 ADCs, CAEN, Italy) that were connected to a computer using the ORCA software package (Department of Physics, University of North Carolina) (Miyaoka et al. 2010).

A specialized multi-point collimated source array was built to expedite the calibration of the cMiCE detector modules. This device holds sixteen ^{22}Na point sources (Isotope Products Laboratories, Valencia, CA.) in a 4×4 square grid with a grid spacing of 12.16 mm. The device has sixteen collimators and sixteen coincidence detectors, one for each point source. This results in sixteen collimated beams that are emitted from the device, each with a beam width of 0.52 mm FWHM at the entrance surface of the cMiCE detector crystal.

The sixteen-beam source was stepped in intervals of 1.013 millimeters, resulting in 49×49 unique beam positions on the entrance face of the detector. For each detected photon coincidence event, Anger positioning was performed to determine the beam that generated that event.

For each (x,y)-beam position, the data from that beam position was histogrammed and an energy window was created that had a lower threshold of 5/6 the photopeak energy (halfway to the Compton edge) and an upper threshold of the photopeak energy plus 1.25 times the full width at tenth max of the photopeak to filter the 1,274 KeV photons from the ^{22}Na source.

The data was then separated into two sets with equal numbers of events, one for calibration of the position estimator (Section 2.4), and the other for testing the positioning algorithm. We refer to these data sets as the calibration set and the testing set.

The calibration data set was then subjected to a further Anger positioning mask for scatter rejection, as described in (Miyaoka et al. 2010). The calibration data at each (x,y)-position was then separated into 4 depth bins (z-positions) by fitting a 2D Lorentzian function to each event and assigning the depth based on the parameters of the best-fit Lorentzian. This was done by clustering the Lorentzian fit parameters so that each cluster had one-fourth of the total number of counts. Thus the depth-bins are of different physical sizes, with smaller bins near the entrance face where more photons are absorbed. This resulted in event data from $49 \times 49 \times 4$ (x,y,z) detector position bins.

This entire process was repeated using a second cMiCE detector module. We will refer to the two modules as Module A and Module B. The full details of the data collection process, depth separation method, and positioning algorithm can be found in (Ling et al. 2007), (Ling et al. 2006), (Miyaoka et al. 2007), and (Miyaoka et al. 2010).

2.3. Simulated Multiplexing of the cMiCE Measured Data

Programs were written in MATLAB (The Mathworks, Inc., Natick, MA, USA) to simulate multiplexing of the calibration and testing datasets. The simulated multiplexing was performed by taking linear combinations of the 64-channel PMT data. No noise or other physical phenomena were modeled in the computation of the multiplexed output signals. The multiplexed calibration and testing datasets were then entered into the workflow as illustrated in Figure 1. The multiplexing schemes simulated are described here:

A. **No Multiplexing:** We used all 64 channels of the measured data with no multiplexing.

B. **RC16:** This multiplexing scheme is standard row/column summation as illustrated in Figure 2a. There are 16 output channels, 8 for the summed signal of each row and 8 for the summed signal for each column.

C. **RC10:** This is a modification of standard row/column summation, where a pair of two spatially separated rows (columns) are summed together into a single channel. This is done to three pairs of rows and three pairs of columns, reducing the number of row and column channels to 5 each, for a total of 10 output channels. This multiplexing scheme is illustrated in Figure 2b.

D. **RC8:** Another modification of row/column summation similar to RC10 with one additional pair of rows and one additional pair of columns being summed together. This results in 4 row channels and 4 column channels for 8 total output channels. This multiplexing scheme is illustrated in Figure 2c.

E. **Mod 3-5 (16):** In this multiplexing scheme, each element of the first column of the detector is on a different output channel: [1,2,3,4,5,6,7,8]. In the second column, the number of the channels is a circular rotation (by three elements) of the first channel: [6,7,8,1,2,3,4,5]. The 3-element rotation is then repeated for successive

columns, creating eight output channels as shown in Figure 2d. We then create eight more channels by repeating this process with a -3 element rotational shift (equivalent to a shift of +5 elements) also shown in Figure 2d.

F.   Mod RC+Edge (19): This multiplexing scheme uses standard row/column summation over the 6×6-element interior of the detector and then adds seven more channels in a ring around the outermost edge of the detector. This multiplexing scheme is illustrated in Figure 2e.

G.   PCA16: This multiplexing scheme is generated by the principal components (Pearson 1901), (Hotelling 1933) of the collected data. For each of the 49×49×4 beam positions in the 64-channel calibration dataset, the number of interaction events at that position was counted. The minimum number of counts from any beam position, n_{min}, was recorded. We then created a new dataset by randomly sampling n_{min} events from each of the $49 \times 49 \times 4$ positions to ensure that each position had an equal number of representative events.

The principal components of the minimally-sampled dataset were then computed. We then used the sixteen principal components corresponding to the sixteen largest singular values as real-valued weightings for multiplexing channels. Figure 3 shows the first fifteen principal components of the data from detector module B.

Each of the 16 multiplexed output channels represent the inner product of the 64-element PMT signal with one of the principal components of the calibration dataset.

H.   PCA16 Snapped: This multiplexing scheme is similar to PCA16, with the exception that the principal component weights for each element were rounded to the nearest 0.1.

I.   PCA16 Swapped: This multiplexing scheme is similar to PCA16, with the exception that the principal components for Detector Module B were used to multiplex the data for Detector Module A. This was repeated vice versa.

J.   (J through O): We repeated the (G) PCA16, (H) PCA16 Snapped, and (I) PCA16 Swapped schemes by using only eight principal components, naming them (J) PCA8, (K) PCA8 Snapped, and (L) PCA8 Swapped. This was done again using only four principal components for the schemes named (M) PCA4, (N) PCA4 Snapped, and (O) PCA4 Swapped.

2.4. Positioning the Multiplexed Event Data

For each (x,y,z)-position of the calibration dataset, the calibration data was multiplexed (via simulation) according to one of the multiplexing schemes described in Section 2.3. The mean and standard deviation of the multiplexed calibration data for that position was recorded to create a lookup table of $49 \times 49 \times 4 \times n$ mean values and another lookup table of $49 \times 49 \times 4 \times n$ standard deviation values, where n is the number of output channels for that multiplexing scheme.

Both the mean and standard deviation lookup tables were then linearly extrapolated in the x and y-directions to $51 \times 51 \times 4 \times n$, approximately 1 mm off of the edge of the crystal. This was followed by a four-fold linear interpolation in the x and y-directions to yield tables that were $201 \times 201 \times 4 \times n$, which were then smoothed in the x and y directions. The details of the mean and standard deviation lookup table creation are generated are given in (Miyaoka et al. 2010).

For each (x,y)-position, the testing dataset for that position was then multiplexed via a MATLAB simulation using the same scheme and each event in the testing dataset was then subjected to a Gaussian Maximum Likelihood (ML) position estimation based on the mean and standard deviation lookup tables. The ML algorithm used has no correlation terms and thus assumes independence of the channels. Events were then binned into a $201 \times 201 \times 4$ histogram according to their maximum likelihood. Events that were positioned off the edge of the detector (into the extrapolated region) were discarded (those histogram bins were set to zero). The details of the ML positioning algorithm can be found in (Ling et al. 2006) and (Miyaoka et al. 2010)

2.5. Computation of Detector Resolution and Bias

For each (x,y)-position, the $201 \times 201 \times 4$ event positioning histogram was summed along the z-direction, resulting in a 201×201 event positioning histogram in x and y only. This histogram was then partitioned into nine regions: four 'corner' regions, each 6×6 mm ; four 'edge' regions, each 6×38 mm along the edges of the detector between the corner regions, and one 'center' region 38×38 mm. We then computed the resolution and bias of the positioned events for each region:

Central Region—For each beam position within the central region of the crystal, profiles were drawn through the max value of the histogram in the x and y directions. The FWHM was computed from these profiles ($FWHM_x$ and $FWHM_y$). For each beam position in the center region, we also computed the bias of the (x,y)-position histogram by computing the centroid of the histogram and recording the mean absolute difference in x and y ($bias_x$ and $bias_y$) to the known beam position.

Edge Regions—For each beam position within an edge region, the 'tangential' resolution ($FWHM_t$) and 'radial' resolution ($FWHM_r$) were computed by drawing profiles through the histogram max parallel to and perpendicular to the detector edge respectively (x and y profiles only). The FWHM was computed from each profile. The absolute bias in the tangential and radial directions ($bias_t$ and $bias_r$) are computed using the same conventions.

Corner Regions—For each beam position within a corner region, the 'tangential' resolution ($FWHM_t$) and 'radial' resolution ($FWHM_r$) is measured by computing the FWHM on a profiles drawn diagonally at 45° and 135° through the histogram max. The tangential and radial bias ($bias_t$ and $bias_r$) were computed for these regions as the distance from the histogram centroid to the 45° and 135° lines through the histogram max.

The mean and standard deviation of the FWHM and bias measurements were computed over all beam positions within each region and the results reported in Table 1 and Table 2.

3. Results

For the computation of the principal components, the minimum number of events from a single position was 412 for module A and 332 for module B. The FWHM and bias measurements for each metric, module, and multiplexing scheme are given in Table 1 and Table 2. We show the half-max contour map for positioning for module B without multiplexing in Figure 4. Contour maps of only the upper-right quadrant of module B for the No Multiplexing, RC16, PCA16, and PCA8 experiments are shown in Figure 5. To avoid clutter in the contour maps, only every other beam position in *x* and *y* are shown (only one-fourth of the total number of beam positions). Anecdotally, we found that module B had a bias in one corner (likely due to an optical aberration) when using the RC16 method. However, this bias was greatly reduced when using the PCA16 method.

4. Discussion

4.1. Experimental Data Collection

We note that an image-based resolution comparison would be useful, but such a comparison is beyond the scope of the current effort. Another limitation of this study is that is does not consider the impact of high countrates on pile-up and dead-time. However, such a study will depend to some extent on the implemented acquisition electronics, so it is beyond the scope of the current study.

Both modules used in this experiment exhibited localized irregularities in the positioning maps. One example can be seen near the bottom-left corner of module B, shown in Figure 4. In one region, events were biased away from the beam regardless of the multiplexing scheme used. The cause of the anomaly is likely due to irregular coupling between the crystal and photocathode or other optical anomaly. A strong bias away from the bottom edge was also present in module B, as seen in Figure 4. We believe this to be caused by loss of light absorption due to the paint peeling away from that edge of the scintillation crystal. In every case, positioning was best at the center of the module and degraded near the edges, especially near the corners. Another issue with the dataset was photon events that were not positioned with the correct source within the 4×4 collimated grid of sources. This led to increased bias away from the beam position.

Due to the fact that the datasets used did not include depth-information, we cannot estimate the depth-of-interaction resolution for this dataset based on our depth separation algorithm alone. Future work will include obtaining new datasets that use a single point source beam and that include depth information from the beam itself (by illuminating the module from the side or using a beam that is slanted from the detector face).

4.2. Using Principal Components for Data Compression

For both modules, the PCA16 multiplexing scheme performed as well as or better than using all 64 channels. This is likely due to the fact that signals obtained by using principal component methods appeared more Gaussian than signals obtained from the uncompressed signals, and thus more suited to the Gaussian ML positioning algorithm. However, even the principal component schemes lost their Gaussian characteristics near the edge and corners.

Future work will investigate using the principal components of only the data from the edges and corners of the modules as additional data channels.

As expected, we saw a degradation of positioning with decreasing number of output channels. However, the PCA4 method still achieved a reasonable resolution in the center of the crystal, but the biases near the edge were large. Thus, the PCA4 method could be a viable multiplexing scheme for the cMiCE modules. However, we do not have an indication of how PCA4 would perform regarding depth-of-interaction. Further experiments will address this issue as investigating the resolution properties as a function of the number of principal components used.

Visual inspection of the principal components from module A and module B reveal that they are very similar. However, the order of components 4 and 5 was reversed and we believe that this was the cause of the bias seen in the PCA4 scheme in module A, and PCA4 Swapped in Module B. We also noticed that when taking random sub-samples of the calibration beam data, the principal component weights did not change with the sub-samples taken. Indeed, the principal components of the two modules were nearly identical even along the edge where we believe the paint had peeled away from one of the crystals and in regions where one module exhibited optical irregularities. We conclude that the principal component weights are robust against anomalies in the data used to compute them.

The fact that the principal components did not change due to data sampling changes, optical irregularities, or even between different modules could have additional benefits. One benefit would be that the principal components could be computed from the calibration beam data of a single module and a multiplexing circuit built according to the weights of those principal components. Since we expect the principal components of the other modules to be nearly identical to the first, we could use the same multiplexing circuit with the same signal weights on all other modules. This would circumvent the need to create individualized multiplexing circuit weights for each module. A set of principal component weights from one module could be used as a template to multiplex all other modules.

Rounding the principal component signal weights to the nearest 0.1 had little effect on the ability to decode photon positions. Tables 1 and 2 show that the FWHM and bias measurements are nearly identical between the computed and the rounded signal weight multiplexing schemes. This proved true when using 16, 8, and even 4 principal components for multiplexing.

Also, rounding to the nearest 0.1 allows for ease of implementation, using only seven channel weights with values $\{-0.3, -0.2, \ldots, +0.2, +0.3\}$, rather than sixty-four different real-valued weights. This will be of benefit if the scheme is to be implemented with a resistive network, since only three resistor values need to be used. Zero-weighted channels account for nearly 25% of all output channels, and these would not require a resistor at all. The negative channels weights would be achieved using inverters with resistances applied to the inverted channels. Thus only relative resistances of 0.1, 0.2, and 0.3 would physically be present in the circuit. Simplifying the circuit in this way is similar to the method in (Siegel et al. 1996).

We see that near the edge of the detectors and the corners, large positioning biases are apparent in both modules. In both modules, the biases at the edge and corners are nearly equal to the FWHM in those regions. However, when comparing the bias of the non-multiplexed signal to the bias of the RC16, PCA16, and PCA8 schemes, we see that the biases are comparable, with slight bias increases when using fewer output channels.

The biases in the edge regions for the PCA4 scheme in module B were slightly higher than that from other multiplexing schemes for that module. It was much higher in the corners of the detectors. However, there was a significant increase in the bias for the PCA4 scheme in module A. We believe that this bias increase is due to the fact that principal components 4 and 5 were reversed between modules A and B. When swapping the principal components for modules A and B (the PCA4 swapped experiments), Tables 1 and 2 show that the biases correspond to the principal components used.

While the principal component methods did perform well under this simulation, its real-world performance remains to be seen. If implemented in a resistive circuit, we believe that the effects of electronic noise introduced by the principal component circuit would be negligible compared to the noise from the signal itself. If implemented in a capacitative circuit, timing resolution would likely be altered. However, the PMT used in cMiCE modules has a summed signal channel that is used for timing, bypassing this issue. The weights of the channels are relative, allowing for a wide selection of parameters among resistor values, buffer amplifiers, etc., that will be determined during the circuit design phase. Attempts to model the noise parameters would be beyond the scope of this paper, and we will investigate this during the circuit design phase.

Finally, we note that at no point in the experiment did the principal component multiplexing method consider the nature of the input signal. We believe that using the principal components of the uncompressed signal can be applied to many different detector configurations, including those that utilize pixelated crystals or light sharing schemes.

4.3. Other Multiplexing Schemes

We found that the Mod 3-5 multiplexing scheme showed poor resolution and large biases even in the center of the crystal. The RC10 and RC8 multiplexing schemes had FWHM measurements similar to other methods with comparable outputs, but showed higher bias than the principal component PCA8 method. The RC8 method had a very large bias in the center region of the crystal.

We found the the Mod RC+Edge method (with 19 output signals) performed well, having FWHM and bias measurements similar to RC16 and PCA16. It showed slightly less bias in the corner regions than PCA16, but had slightly larger FWHM measurements in the center and edge regions.

5. Conclusion

We conclude from this work that the principal component multiplexing schemes presented are worthy of further investigation. Our goal for the near future will be to construct these

circuits and analyze their performance in the presence of real-world noise. We will also investigate using different combinations of principal components, and principal components from localized regions of the detectors.

If viable, principal component multiplexing schemes could maintain acceptable positioning with a minimal number of output channels. This would reduce construction costs with minimal impact on scanner performance.
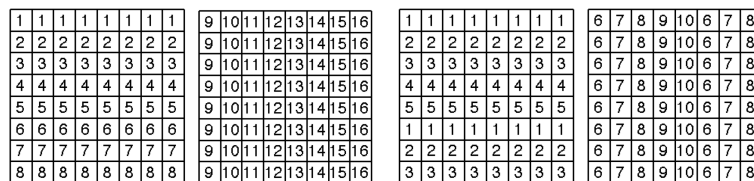
Acknowledgments

References

Bruyndonckx P, Lemaitre C, van der Laan D, Maas M, Schaart D, Devroede O, Krieguer M, Tavernier S. Nuclear Science Symposium Conference Record, 2006 IEEE. 2006; 4:2518–2522.

Bruyndonckx P, Leonard S, Tavernier S, Lemaitre C, Devroede O, Wu Y, Krieguer M. IEEE TRANSACTIONS ON NUCLEAR SCIENCE. 2004; 51(5, 2):2520–2525.

Casey M, Nutt R. Nuclear Science, IEEE Transactions on. 1986; 33(1):460–463.

Dahlbom M, Hoffman E. Medical Imaging, IEEE Transactions on. 1988; 7(4):264–272.

DeWitt D, Johnson-Williams NG, Miyaoka RS, Li X, Lockhart C, Lewellen TK, Hauck S. IEEE TRANSACTIONS ON NUCLEAR SCIENCE. 2010; 57(1, 1):71–77. [PubMed: 21197135]

Downie E, Yang X, Peng H. PHYSICS IN MEDICINE AND BIOLOGY. 2013; 58(11):3943–3964. [PubMed: 23680653]

Hotelling H. JOURNAL OF EDUCATIONAL PSYCHOLOGY. 1933; 24:417–441.

Joung J, Miyaoka R, Lewellen T. NUCLEAR INSTRUMENTS & METHODS IN PHYSICS RESEARCH SECTION A-ACCELERATORS SPECTROMETERS DETECTORS AND ASSOCIATED EQUIPMENT. 2002; 489(1-3):584–598.

Karp J, Muehllehner G, Beerbohm D, Mankoff D. Nuclear Science, IEEE Transactions on. 1986; 33(1):550–555.

Lerche C, Benlloch J, Sanchez F, Pavon N, Escat B, Gimenez E, Fernandez M, Torres I, Gimenez M, Sebastia A, Martinez J. Nuclear Science, IEEE Transactions on. 2005; 52(3):560–572.

Li X, Lockhart C, Lewellen TK, Miyaoka RS. IEEE TRANSACTIONS ON NUCLEAR SCIENCE. 2011; 58(3, 1):590–596. [PubMed: 22685348]

Li X, Lockhart C, Lewellen T, Miyaoka R. Engineering in Medicine and Biology Society, 2008 EMBS 2008 30th Annual International Conference of the IEEE. 2008:2287–2290.

Ling T, Burnett TH, Lewellen TK, Miyaoka RS. PHYSICS IN MEDICINE AND BIOLOGY. 2008; 53(7):1843–1863. [PubMed: 18364542]

Ling T, Lee K, Miyaoka RS. IEEE TRANSACTIONS ON NUCLEAR SCIENCE. 2006; 53(5, 1): 2513–2518.

Ling T, Lewellen TK, Miyaoka RS. PHYSICS IN MEDICINE AND BIOLOGY. 2007; 52(8):2213–2228. [PubMed: 17404465]

Maas MC, Schaart DR, van der Laan DJJ, Bruyndonckx P, Lematre C, Beekman FJ, van Eijk CWE. Physics in Medicine and Biology. 2009; 54(7) 1893. URL: http://stacks.iop.org/0031-9155/54/i=7/a=003.

Marone A, Fiorini C, Baraldi P, Cadini F, Zio E, Camera F. Nuclear Science Symposium Conference Record (NSS/MIC), 2009 IEEE. 2009:645–649.

Miyaoka RS, Li X, Hunter W, Pierce LA II, McDougald W, Kinahan PE, Lewellen TK. IEEE TRANSACTIONS ON NUCLEAR SCIENCE. 2011; 58(5, 1):2244–2249.

Miyaoka RS, Ling T, Lewellen TK. IEEE TRANSACTIONS ON NUCLEAR SCIENCE. 2007; 54(5, 1):1561–1567. [PubMed: 19180248]

Miyaoka RS, Ling T, Lockhart C, Li X, Lewellen TK. IEEE TRANSACTIONS ON NUCLEAR SCIENCE. 2010; 57(3, 1):1023–1028.

Olcott P, Chinn G, Levin C. Nuclear Science Symposium and Medical Imaging Conference (NSS/MIC), 2011 IEEE. 2011:3224–3226.

Pearson K. PHILOSOPHICAL MAGAZINE. 1901; 2(7-12):559–572.

Picard Y, Thompson C. Nuclear Science, IEEE Transactions on. 1994; 41(4):1464–1468.

Schaart DR, van Dam HT, Seifert S, Vinke R, Dendooven P, Lhner H, Beekman FJ. Physics in Medicine and Biology. 2009; 54(11):3501. URL: http://stacks.iop.org/0031-9155/54/i=11/a=015.

Shih Y, Sun FW, MacDonald L, Otis B, Miyaoka R, McDougald W, Lewellen T. Nuclear Science Symposium Conference Record (NSS/MIC), 2009 IEEE. 2009:2376–2380.

Siegel S, Silverman R, Shao Y, Cherry S. Nuclear Science, IEEE Transactions on. 1996; 43(3):1634–1641.

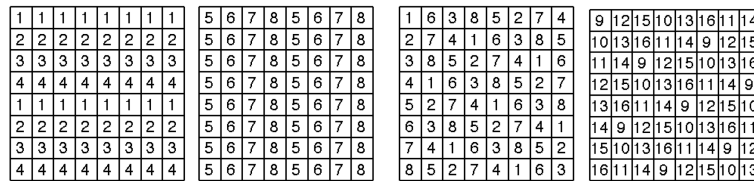Tanaka E, Hiramoto T, Nohara N. Journal of Nuclear Medicine. 1970; 11(9):542. [PubMed: 5505223]
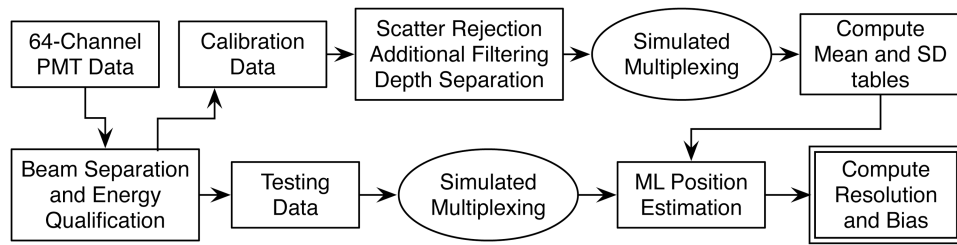
Figure 1.
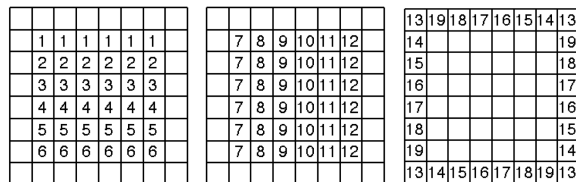Diagram of the workflow described in (Miyaoka et al. 2010) with the addition of simulated multiplexing.

RC16 left grid:

1	1	1	1	1	1	1	1
2	2	2	2	2	2	2	2
3	3	3	3	3	3	3	3
4	4	4	4	4	4	4	4
5	5	5	5	5	5	5	5
6	6	6	6	6	6	6	6
7	7	7	7	7	7	7	7
8	8	8	8	8	8	8	8

RC16 right grid:

9	10	11	12	13	14	15	16
9	10	11	12	13	14	15	16
9	10	11	12	13	14	15	16
9	10	11	12	13	14	15	16
9	10	11	12	13	14	15	16
9	10	11	12	13	14	15	16
9	10	11	12	13	14	15	16
9	10	11	12	13	14	15	16

The RC16 row/column summation. There are 8 signals from row summation (left) and 8 from column summation (right) for 16 total output channels.

RC10 left grid:

1	1	1	1	1	1	1	1
2	2	2	2	2	2	2	2
3	3	3	3	3	3	3	3
4	4	4	4	4	4	4	4
5	5	5	5	5	5	5	5
1	1	1	1	1	1	1	1
2	2	2	2	2	2	2	2
3	3	3	3	3	3	3	3

RC10 right grid:

6	7	8	9	10	6	7	8
6	7	8	9	10	6	7	8
6	7	8	9	10	6	7	8
6	7	8	9	10	6	7	8
6	7	8	9	10	6	7	8
6	7	8	9	10	6	7	8
6	7	8	9	10	6	7	8
6	7	8	9	10	6	7	8

The RC10 row/column summation. Note that some row and column channels are repeated so that only 10 output channels are shown.

RC8 left grid:

1	1	1	1	1	1	1	1
2	2	2	2	2	2	2	2
3	3	3	3	3	3	3	3
4	4	4	4	4	4	4	4
1	1	1	1	1	1	1	1
2	2	2	2	2	2	2	2
3	3	3	3	3	3	3	3
4	4	4	4	4	4	4	4

RC8 right grid:

| 5	6	7	8	5	6	7	8
5	6	7	8	5	6	7	8
5	6	7	8	5	6	7	8
5	6	7	8	5	6	7	8
5	6	7	8	5	6	7	8
5	6	7	8	5	6	7	8
5	6	7	8	5	6	7	8
5	6	7	8	5	6	7	8

The RC8 row/column summation. Note that some row and column channels are repeated so that only 8 output channels are shown.

MOD 3-5 left grid:

1	6	3	8	5	2	7	4
2	7	4	1	6	3	8	5
3	8	5	2	7	4	1	6
4	1	6	3	8	5	2	7
5	2	7	4	1	6	3	8
6	3	8	5	2	7	4	1
7	4	1	6	3	8	5	2
8	5	2	7	4	1	6	3

MOD 3-5 right grid:

9	12	15	10	13	16	11	14
10	13	16	11	14	9	12	15
11	14	9	12	15	10	13	16
12	15	10	13	16	11	14	9
13	16	11	14	9	12	15	10
14	9	12	15	10	13	16	11
15	10	13	16	11	14	9	12
16	11	14	9	12	15	10	13

The MOD 3-5 multiplexing scheme. Each column of the left figure is a +3 rotational shift of the previous column. A rotational shift of -3 is applied to the columns of the figure on the right for an additional 8 output channels.

MOD RC+edge, left figure (interior rows):

	1	1	1	1	1	1	
	2	2	2	2	2	2	
	3	3	3	3	3	3	
	4	4	4	4	4	4	
	5	5	5	5	5	5	
	6	6	6	6	6	6	

MOD RC+edge, center figure (interior columns):

	7	8	9	10	11	12	
	7	8	9	10	11	12	
	7	8	9	10	11	12	
	7	8	9	10	11	12	
	7	8	9	10	11	12	
	7	8	9	10	11	12	

MOD RC+edge, right figure (edge ring):

| 13	19	18	17	16	15	14	13
14							19
15							18
16							17
17							16
18							15
19							14
13	14	15	16	17	18	19	13

The MOD RC+edge multiplexing scheme. The left figure shows the six channels that sum the interior rows. The center figure shows the six channels that sum the interior columns. The figure at right shows seven additional channels in a ring around the edge of the detector module for a total of 19 output channels.
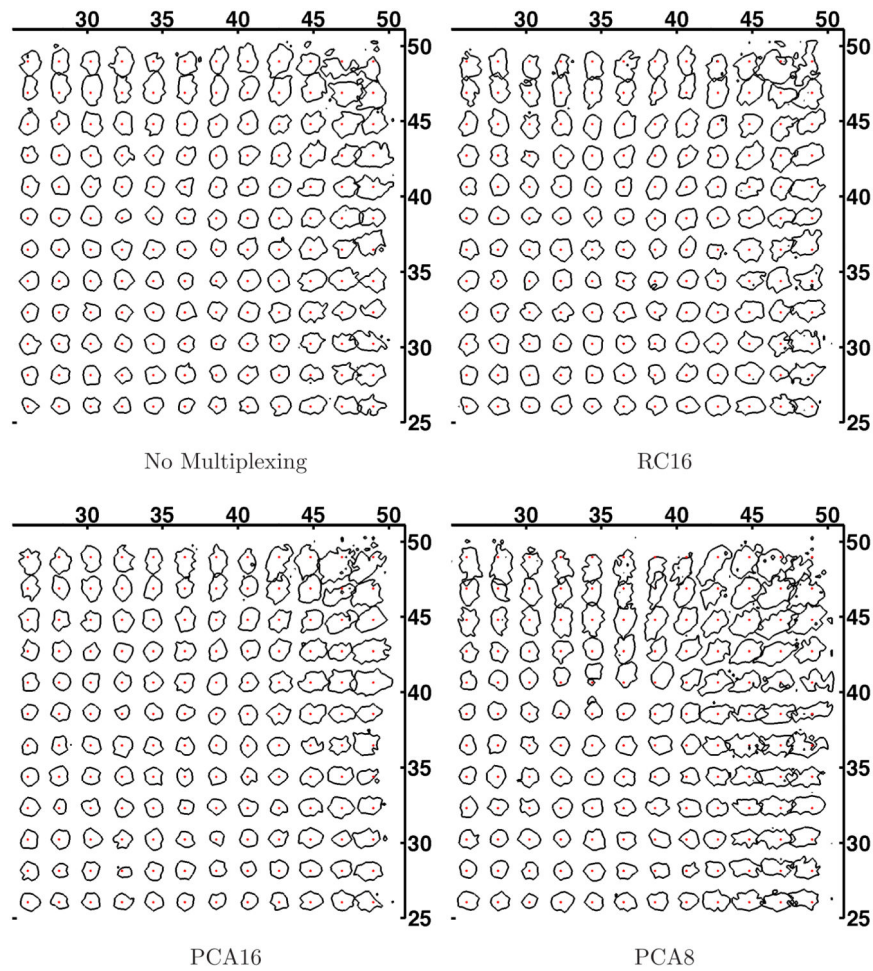
Figure 2.
Illustrations of the various multiplexing schemes used. Each image shows an 8×8 array representing the PMT output channels. For each scheme, the channels with the same numbered label are summed together for multiplexing. Thus, each number represents a single output channel for the multiplexing scheme.
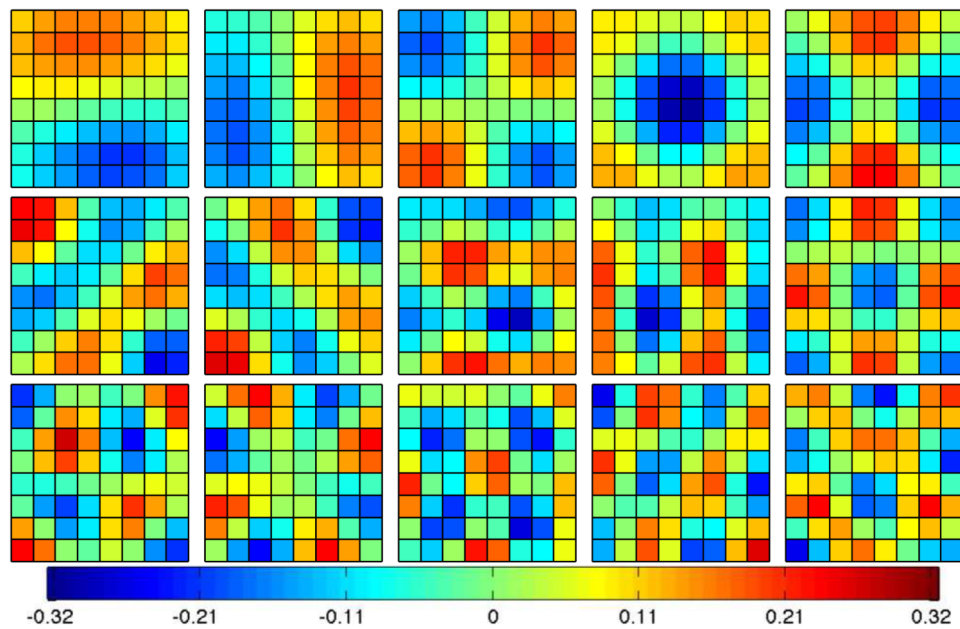
Figure 3.
Colormaps of the first 15 (orthonormal) principal component vectors of the data from Detector Module B. The images are ordered according to the order of the corresponding singular values $\{\lambda_1 > \lambda_2 > \ldots > \lambda_{64}\}$. The top row (from left to right) shows the vectors corresponding to $\{\lambda_1, \lambda_2, \ldots\}$ (the largest singular values), the second row corresponds to $\{\lambda_6, \lambda_7, \ldots\}$, and so on. Each principal component was used as an output channel by weighting the 64-channel PMT signal according to the color scheme for that principal component.
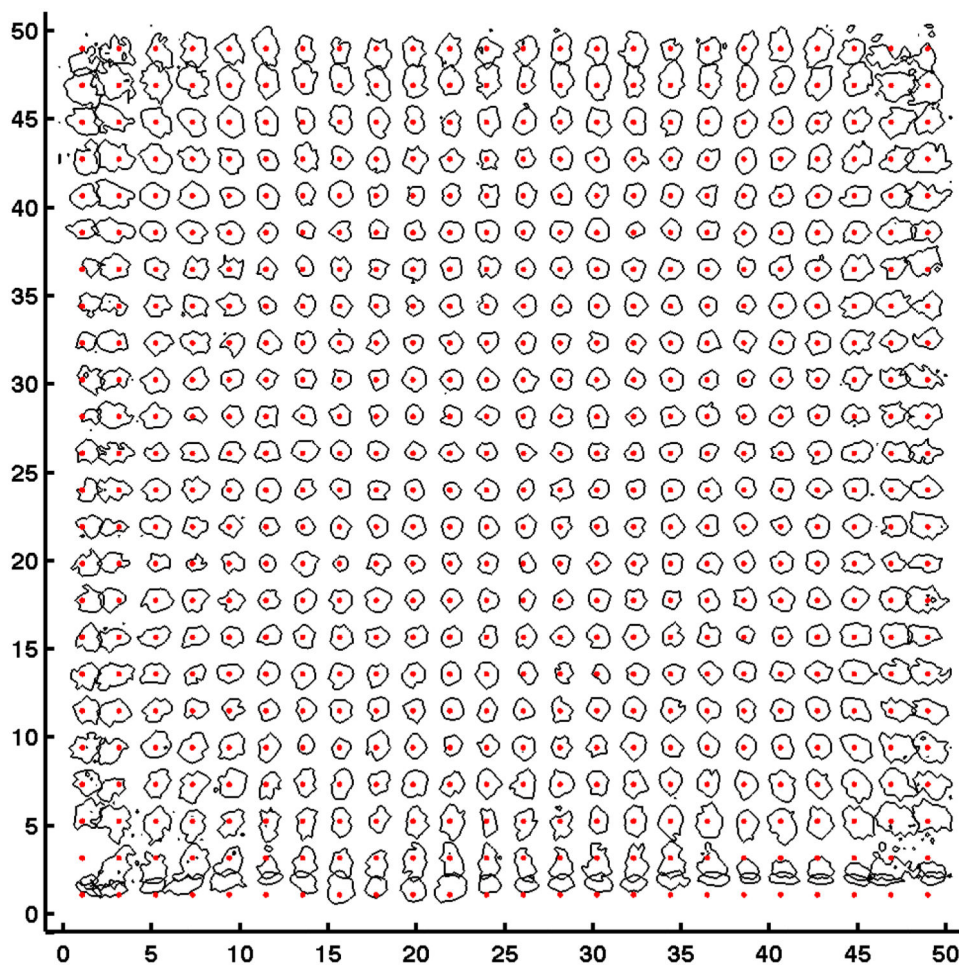
Figure 4.
Half-max contours for positioning with no multiplexing for module B. Red dots indicate the true beam positions. We believe the strong upward bias along the bottom edge to be a result of paint peeling away from the edge of the crystal. We believe that the anomaly near the bottom-left is due to issues with the optical coupling of the scintillator to the PMT. A zoomed view of the upper-right quadrant is shown in Figure 5

Figure 5.
Half-max contours for the No Multiplexing, RC 16, PCA 16, and PCA 8 multiplexing schemes. Only the upper-right quadrant of the crystal is shown.

Table 1

Resolution and bias results for Module A for 15 multiplexing schemes. Horizontal lines separate multiplexing schemes into groups with the same number of output channels. Entries are mean ± standard deviation. All units are millimeters.

Module A

	Center		Edge		Corner	
	$FWHM_x$	$FWHM_y$	$FWHM_r$	$FWHM_t$	$FWHM_r$	$FWHM_t$
No Mult	1.17 ± 0.18	1.20 ± 0.19	1.50 ± 0.41	1.22 ± 0.26	1.43 ± 0.55	1.29 ± 0.51
Mod RCE	1.20 ± 0.20	1.24 ± 0.20	1.55 ± 0.39	1.27 ± 0.27	1.38 ± 0.63	1.23 ± 0.52
RC16	1.18 ± 0.20	1.25 ± 0.22	1.66 ± 0.42	1.22 ± 0.28	1.45 ± 0.64	1.21 ± 0.53
PCA16	1.19 ± 0.18	1.17 ± 0.18	1.50 ± 0.34	1.20 ± 0.23	1.62 ± 0.64	1.27 ± 0.46
PCA16 SN	1.21 ± 0.17	1.16 ± 0.18	1.50 ± 0.34	1.21 ± 0.22	1.54 ± 0.66	1.23 ± 0.41
PCA16 SW	1.18 ± 0.17	1.16 ± 0.18	1.51 ± 0.34	1.19 ± 0.22	1.59 ± 0.58	1.30 ± 0.48
Mod 3-5	1.28 ± 0.29	1.31 ± 0.29	1.68 ± 0.47	1.31 ± 0.28	1.53 ± 0.66	1.31 ± 0.50
RC10	1.25 ± 0.21	1.27 ± 0.21	1.69 ± 0.41	1.26 ± 0.28	1.59 ± 0.70	1.24 ± 0.60
RC8	1.29 ± 0.25	1.31 ± 0.23	1.65 ± 0.42	1.33 ± 0.83	1.56 ± 0.65	1.26 ± 0.54
PCA8	1.26 ± 0.22	1.24 ± 0.21	1.78 ± 0.51	1.20 ± 0.27	1.76 ± 0.76	1.38 ± 0.59
PCA8 SN	1.27 ± 0.21	1.27 ± 0.23	1.78 ± 0.54	1.20 ± 0.26	1.68 ± 0.67	1.41 ± 0.62
PCA8 SW	1.24 ± 0.22	1.21 ± 0.22	1.81 ± 0.50	1.20 ± 0.27	1.78 ± 0.74	1.38 ± 0.53
PCA4	1.47 ± 0.75	1.30 ± 0.43	2.03 ± 1.32	1.23 ± 0.53	1.62 ± 0.83	1.45 ± 0.68
PCA4 SN	1.57 ± 0.67	1.32 ± 0.44	2.07 ± 1.35	1.26 ± 0.50	1.70 ± 0.73	1.46 ± 0.78
PCA4 SW	1.30 ± 0.28	1.29 ± 0.29	1.80 ± 0.62	1.42 ± 0.58	1.29 ± 0.70	1.17 ± 0.96

	Center		Edge		Corner	
	$Bias_x$	$Bias_y$	$Bias_r$	$Bias_t$	$Bias_r$	$Bias_t$
No Mult	0.16 ± 0.12	0.18 ± 0.14	1.10 ± 0.79	0.16 ± 0.16	1.40 ± 1.07	0.53 ± 0.46
Mod RCE	0.16 ± 0.12	0.18 ± 0.14	1.07 ± 0.78	0.16 ± 0.16	1.42 ± 1.13	0.53 ± 0.47
RC16	0.17 ± 0.14	0.19 ± 0.15	1.13 ± 0.80	0.17 ± 0.17	1.45 ± 1.11	0.54 ± 0.46

Module A

PCA16	0.16 ± 0.12	0.18 ± 0.13	1.14 ± 0.77	0.16 ± 0.14	1.49 ± 0.97	0.48 ± 0.43
PCA16 SN	0.16 ± 0.12	0.18 ± 0.13	1.15 ± 0.77	0.16 ± 0.14	1.50 ± 1.00	0.48 ± 0.43
PCA16 SW	0.16 ± 0.12	0.17 ± 0.13	1.14 ± 0.77	0.16 ± 0.14	1.47 ± 0.97	0.47 ± 0.42
Mod 3-5	2.76 ± 2.09	2.75 ± 2.04	1.74 ± 0.80	0.54 ± 0.42	1.60 ± 1.15	0.54 ± 0.48
RC10	0.28 ± 0.22	0.26 ± 0.20	1.38 ± 0.86	0.20 ± 0.18	1.89 ± 1.26	0.55 ± 0.50
RC8	1.30 ± 1.04	1.04 ± 0.88	1.35 ± 0.81	1.21 ± 1.16	1.84 ± 1.22	0.51 ± 0.48
PCA8	0.16 ± 0.12	0.18 ± 0.13	1.20 ± 0.78	0.16 ± 0.14	1.58 ± 1.00	0.50 ± 0.44
PCA8 SN	0.16 ± 0.11	0.19 ± 0.13	1.20 ± 0.78	0.16 ± 0.14	1.61 ± 1.03	0.50 ± 0.44
PCA8 SW	0.17 ± 0.12	0.18 ± 0.13	1.17 ± 0.77	0.16 ± 0.14	1.50 ± 0.98	0.50 ± 0.44
PCA4	0.17 ± 0.13	0.27 ± 0.31	2.37 ± 2.16	0.25 ± 0.20	1.73 ± 1.03	0.61 ± 0.48
PCA4 SN	0.18 ± 0.13	0.31 ± 0.30	2.30 ± 2.10	0.25 ± 0.21	1.75 ± 1.10	0.62 ± 0.50
PCA4 SW	0.15 ± 0.12	0.18 ± 0.13	1.16 ± 0.75	0.19 ± 0.19	1.77 ± 1.15	0.75 ± 0.59

Table 2

Resolution and bias results for Module B for 15 multiplexing schemes. Horizontal lines separate multiplexing schemes into groups with the same number of output channels. Entries are mean ± standard deviation. All units are millimeters.

Module B

	Center		Edge		Corner	
	$FWHM_x$	$FWHM_y$	$FWHM_r$	$FWHM_t$	$FWHM_r$	$FWHM_t$
No Mult	1.12 ± 0.17	1.14 ± 0.19	1.46 ± 0.38	1.20 ± 0.24	1.40 ± 0.51	1.27 ± 0.42
Mod RCE	1.16 ± 0.18	1.17 ± 0.20	1.51 ± 0.40	1.22 ± 0.24	1.47 ± 0.62	1.18 ± 0.43
RC16	1.16 ± 0.19	1.19 ± 0.22	1.56 ± 0.39	1.20 ± 0.26	1.51 ± 0.64	1.16 ± 0.39
PCA16	1.12 ± 0.16	1.11 ± 0.17	1.46 ± 0.34	1.13 ± 0.20	1.69 ± 0.53	1.18 ± 0.37
PCA16 SN	1.13 ± 0.16	1.12 ± 0.16	1.44 ± 0.33	1.13 ± 0.20	1.65 ± 0.54	1.19 ± 0.38
PCA16 SW	1.12 ± 0.16	1.10 ± 0.17	1.44 ± 0.32	1.13 ± 0.19	1.61 ± 0.45	1.18 ± 0.35
Mod 3-5	1.24 ± 0.25	1.22 ± 0.26	1.60 ± 0.44	1.24 ± 0.26	1.44 ± 0.54	1.18 ± 0.50
RC10	1.20 ± 0.20	1.20 ± 0.20	1.61 ± 0.40	1.23 ± 0.25	1.53 ± 0.59	1.21 ± 0.46
RC8	1.25 ± 0.21	1.23 ± 0.21	1.58 ± 0.41	1.36 ± 1.51	1.48 ± 0.53	1.19 ± 0.49
PCA8	1.17 ± 0.22	1.16 ± 0.23	1.75 ± 0.52	1.13 ± 0.25	1.91 ± 0.75	1.28 ± 0.42
PCA8 SN	1.18 ± 0.22	1.18 ± 0.23	1.73 ± 0.54	1.17 ± 0.28	1.69 ± 0.67	1.38 ± 0.50
PCA8 SW	1.17 ± 0.19	1.17 ± 0.22	1.68 ± 0.51	1.12 ± 0.24	1.89 ± 0.67	1.32 ± 0.44
PCA4	1.24 ± 0.29	1.26 ± 0.31	1.75 ± 0.74	1.32 ± 0.48	1.44 ± 0.68	1.28 ± 0.86
PCA4 SN	1.31 ± 0.38	1.31 ± 0.38	1.74 ± 0.74	1.35 ± 0.56	1.42 ± 0.74	1.26 ± 1.08
PCA4 SW	1.31 ± 0.67	1.25 ± 0.45	2.11 ± 1.39	1.20 ± 0.46	1.40 ± 0.74	1.27 ± 0.58

	Center		Edge		Corner	
	$Bias_x$	$Bias_y$	$Bias_r$	$Bias_t$	$Bias_r$	$Bias_t$
No Mult	0.18 ± 0.13	0.17 ± 0.12	1.08 ± 0.80	0.15 ± 0.14	1.25 ± 1.04	0.49 ± 0.46
Mod RCE	0.18 ± 0.14	0.16 ± 0.13	1.06 ± 0.80	0.15 ± 0.15	1.24 ± 1.06	0.50 ± 0.46
RC16	0.18 ± 0.14	0.17 ± 0.13	1.11 ± 0.80	0.15 ± 0.16	1.24 ± 1.02	0.51 ± 0.47

Module B

PCA16	0.17 ± 0.13	0.16 ± 0.12	1.10 ± 0.78	0.15 ± 0.15	1.30 ± 0.91	0.46 ± 0.43
PCA16 SN	0.18 ± 0.13	0.16 ± 0.12	1.10 ± 0.78	0.15 ± 0.15	1.32 ± 0.91	0.46 ± 0.43
PCA16 SW	0.17 ± 0.13	0.16 ± 0.12	1.09 ± 0.76	0.15 ± 0.15	1.30 ± 0.92	0.45 ± 0.42
Mod 3-5	2.86 ± 2.22	2.96 ± 2.28	1.71 ± 0.83	0.54 ± 0.45	1.37 ± 1.14	0.48 ± 0.46
RC10	0.29 ± 0.22	0.30 ± 0.24	1.44 ± 0.87	0.18 ± 0.15	1.69 ± 1.21	0.48 ± 0.45
RC8	1.33 ± 1.10	1.35 ± 1.02	1.39 ± 0.81	1.32 ± 1.24	1.63 ± 1.17	0.45 ± 0.42
PCA8	0.18 ± 0.13	0.17 ± 0.11	1.16 ± 0.78	0.15 ± 0.14	1.38 ± 0.98	0.50 ± 0.45
PCA8 SN	0.19 ± 0.13	0.17 ± 0.12	1.17 ± 0.78	0.15 ± 0.15	1.42 ± 0.99	0.51 ± 0.45
PCA8 SW	0.18 ± 0.13	0.17 ± 0.12	1.16 ± 0.79	0.15 ± 0.15	1.42 ± 0.98	0.50 ± 0.45
PCA4	0.17 ± 0.13	0.16 ± 0.11	1.18 ± 0.76	0.20 ± 0.21	1.72 ± 1.22	0.78 ± 0.62
PCA4 SN	0.17 ± 0.14	0.16 ± 0.12	1.16 ± 0.78	0.23 ± 0.24	1.84 ± 1.24	0.85 ± 0.63
PCA4 SW	0.18 ± 0.14	0.25 ± 0.30	2.13 ± 1.99	0.21 ± 0.16	1.51 ± 1.08	0.58 ± 0.50